

RESEARCH ARTICLE

10.1002/2015JA021211

Statistical characterization of the forenoon particle and wave morphology: ARTEMIS observations

Y. Harada¹, J. S. Halekas², A. R. Poppe¹, Y. Tsugawa³, S. Kurita⁴, and J. P. McFadden¹¹Space Sciences Laboratory, University of California, Berkeley, California, USA, ²Department of Physics and Astronomy, University of Iowa, Iowa City, Iowa, USA, ³Department of Geophysics, Graduate School of Science, Tohoku University, Sendai, Japan, ⁴Solar-Terrestrial Environment Laboratory, Nagoya University, Nagoya, Japan

Key Points:

- ARTEMIS observes a wide variety of lunar upstream particles and waves
- Global distributions of lunar upstream phenomena are organized by IMF direction
- Low-frequency wave distributions are controlled by Mach numbers

Correspondence to:

Y. Harada,
haraday@ssl.berkeley.edu

Citation:

Harada, Y., J. S. Halekas, A. R. Poppe, Y. Tsugawa, S. Kurita, and J. P. McFadden (2015), Statistical characterization of the forenoon particle and wave morphology: ARTEMIS observations, *J. Geophys. Res. Space Physics*, 120, doi:10.1002/2015JA021211.

Received 13 MAR 2015

Accepted 3 JUN 2015

Accepted article online 6 JUN 2015

Abstract Although the zeroth-order picture of the Moon-solar wind interaction involves no upstream perturbation, the presence of the Moon does affect the upstream plasma in a variety of ways. In this paper, a large volume of data obtained by the dual-probe Acceleration, Reconnection, Turbulence and Electrodynamics of the Moon's Interaction with the Sun (ARTEMIS) mission are used to characterize the large-scale morphology of the "forenoon," which is defined as the region upstream of the Moon and its wake that contains Moon-related particles and waves. Solar wind ions reflected from the unshielded surface and by crustal magnetic fields, together with heavy ions of lunar surface/exospheric origin, are picked up by the solar wind magnetic and electric fields. Partially coinciding with populations of these Moon-related ions, ~0.01 Hz and ~1 Hz magnetic field fluctuations are observed. The morphology of the Moon-related ion and wave distributions is well organized by the upstream magnetic field direction. In addition, the low-frequency wave distributions depend on the upstream Alfvén Mach numbers, suggesting that propagation effects also play a role in determining the wave forenoon morphology. Occurrence of modified electron velocity distributions and higher-frequency, electromagnetic, and electrostatic waves is primarily controlled by magnetic connection to the Moon and its wake. These statistical results observationally demonstrate the large-scale properties of the forenoon and upstream-parameter control thereof.

1. Introduction

The Moon-solar wind interaction provides a representative, most studied example of the interaction of an unmagnetized, airless body with flowing plasma [Schubert and Lichtenstein, 1974; Halekas et al., 2011, 2015]. The dayside lunar surface is directly bombarded by the incident charged particles owing to the lack of global magnetic and atmospheric shielding. Early observations suggested that the incoming solar wind plasma is completely absorbed by the Moon with virtually no perturbations in the upstream plasma, leading to the absence of a global bow shock and the formation of the lunar wake, i.e., a plasma void behind the Moon [Colburn et al., 1967; Lyon et al., 1967; Ness et al., 1967]. It was also suggested that the Moon can be treated as a perfect insulator on the zeroth order, so that the interplanetary magnetic field (IMF) is rapidly diffused into the lunar interior without piling up on the Moon's dayside.

Although no upstream perturbation of plasma and fields is expected in this "passive absorber" model, a number of types of Moon-related particles and waves have been observed in the upstream solar wind plasma (Y. Harada and J. S. Halekas, Upstream waves and particles at the Moon, *Geophysical Monograph Series*, unpublished manuscript, 2015). The solar wind ions are reflected up to a few percent from the unmagnetized surface [Saito et al., 2008; Lue et al., 2014] and up to 50% from strongest magnetic anomalies [Saito et al., 2010; Lue et al., 2011]. Multiple species of lunar ions sputtered directly from the surface and/or ionized from the lunar neutral exosphere have been detected as pickup ions in the solar wind [Benson et al., 1975; Hilchenbach et al., 1993; Mall et al., 1998; Yokota et al., 2009; Halekas et al., 2012a]. Surface absorption of electrons combined with magnetic/electrostatic reflection produces loss cones in the upward electron velocity distributions [Anderson et al., 1975]. Field-aligned electron beams upcoming from the Moon are observed both on the dayside [Halekas et al., 2012b; Harada et al., 2014] and in the wake [Halekas et al., 2002]. Also, the wake-related potential drop gives rise to counterstreaming electrons on the field lines piercing the wake [Farrell et al., 1996; Futaana et al., 2001; Halekas et al., 2011].

These additional particle components and modified velocity distributions can generate several classes of waves. Magnetometer measurements by lunar orbiters have revealed the presence of large-amplitude ULF

waves with peak frequencies $\sim 0.01 - 0.1$ Hz [Nakagawa *et al.*, 2012; Halekas *et al.*, 2013], broadband magnetic turbulence at $0.1 - 10$ Hz [Halekas *et al.*, 2008, 2012c; Nakagawa *et al.*, 2011; Tsugawa *et al.*, 2012], and ~ 1 Hz narrowband whistlers [Lin *et al.*, 1998; Halekas *et al.*, 2006, 2008, 2013; Tsugawa *et al.*, 2011]. These low-frequency waves are generally enhanced above strong crustal magnetic fields, implying their association with reflected ions. In contrast, higher-frequency, ~ 100 Hz whistlers are weakened when the field lines are connected to strong crustal fields, suggesting electron anisotropy caused by surface absorption as a plausible free energy source [Harada *et al.*, 2014]. Broadband electrostatic emission is frequently detected on the field lines connected to the Moon or to the lunar wake, as well as inside the wake [Bale *et al.*, 1997; Farrell *et al.*, 1997; Hashimoto *et al.*, 2010; Nishino *et al.*, 2010; Tao *et al.*, 2012; Harada *et al.*, 2014].

Many of the lunar upstream phenomena have similarities to those observed in the planetary and cometary foreshocks [Russell and Hoppe, 1983; Coates and Jones, 2009], though the Moon lacks a global bow shock. For example, magnetic connection to the Moon/wake is a primary factor controlling occurrence of lunar upstream waves as magnetic connection to the bow shock is important for foreshock waves. In this paper, we define the “foremoon” as the region upstream of the Moon and its wake that contains particles and waves associated with the Moon. Our current understanding of the foremoon has been based mostly on event studies and low-altitude statistics. The observational limitation has hindered direct confirmation of large-scale foremoon properties that are extrapolated from the case studies and are predicted by simulations. The aim of this paper is characterization and visualization of the morphology of this foremoon region, where a wide variety of lunar upstream phenomena of ions, electrons, and low- and high-frequency waves are observed. We conduct comprehensive statistics to obtain the global distributions of each type of lunar upstream particles and waves, utilizing a huge volume of data accumulated over 3.5 years by two probes of the Acceleration, Reconnection, Turbulence and Electrodynamics of the Moons Interaction with the Sun (ARTEMIS) mission [Angelopoulos, 2011]. The unprecedented scale of comprehensive data sets from ARTEMIS enables a direct, observational study on the large-scale distributions of many kinds of lunar upstream phenomena. The rest of the paper is structured as follows: section 2 provides a brief description of the ARTEMIS data used in this study. In section 3, we present the statistically derived global distributions of lunar upstream particles and waves in different IMF directions. In section 4, we discuss expected and unexpected features of the statistical results in the context of how these results refine our understanding of the Moon-plasma interaction. Finally, the major conclusions of this paper are provided in section 5.

2. Data Sets

The plasma and field data used in this work were obtained from July 2011 to December 2014 by ESA (electrostatic analyzer) [McFadden *et al.*, 2008], EFI (electric field instrument) [Bonnell *et al.*, 2008], SCM (search coil magnetometer) [Roux *et al.*, 2008], and FGM (fluxgate magnetometer) [Auster *et al.*, 2008] instruments on board ARTEMIS. The ESA instrument measures ions from 1.6 eV to 25 keV and electrons from 2 eV to 32 keV with 4π steradian fields of view. The EFI conducts electric field measurements from DC up to 8 kHz. The SCM provides magnetic field spectra and waveforms from 0.1 Hz to 4 kHz. The FGM measures the magnetic field from DC up to 64 Hz. The two ARTEMIS probes have nearly ecliptic orbits with inclination $\sim 0^\circ - 30^\circ$, periaapsis altitudes $\sim 10 - 1000$ km, and apoapsis altitudes $\sim 9 - 11 R_L$, where the lunar radius $R_L = 1738$ km. We present statistical maps of quantities related to lunar upstream phenomena in the solar wind. We select solar wind intervals based on the Moon's position: $-90^\circ < \phi_{\text{MoonGSE}} < 90^\circ$, where ϕ_{MoonGSE} is the azimuthal angle of the lunar position in the geocentric solar ecliptic (GSE) coordinates. We utilize the dual-probe capability of ARTEMIS by subtracting quantities observed by one probe from those observed by the other probe so that we can minimize contamination from background phenomena such as waves intrinsic in the solar wind and backstreaming particles and waves in the terrestrial foreshock. For example, a dual-probe quantity at P1, $Q_{\text{dual},1} = Q_{\text{single},1} - Q_{\text{single},2}$, is mapped as a function of location of P1, and $Q_{\text{dual},2} = Q_{\text{single},2} - Q_{\text{single},1}$ is mapped as a function of location of P2, where $Q_{\text{single},1}$ and $Q_{\text{single},2}$ are single-probe quantities observed by P1 and P2, respectively. We reject the dual-probe quantities when the other probe (P1 for $Q_{\text{dual},2}$ and P2 for $Q_{\text{dual},1}$) is located in the wake (ion density $< 0.5 \text{ cm}^{-3}$ or spacecraft in the geometric shadow). If we assume that spatial scales of background phenomena are sufficiently large compared to the spacecraft separation $\sim 1 - 10 R_L$, the dual-probe subtraction can remove background contribution. Thus, dual-probe quantities, especially those enhanced near the Moon, can be associated with Moon-related phenomena. In case that both of the two probes simultaneously detect Moon-related signals, they may be canceled out by this procedure. However, lunar signals are typically detected only by one probe in the ARTEMIS data. This is because periaapsis timings

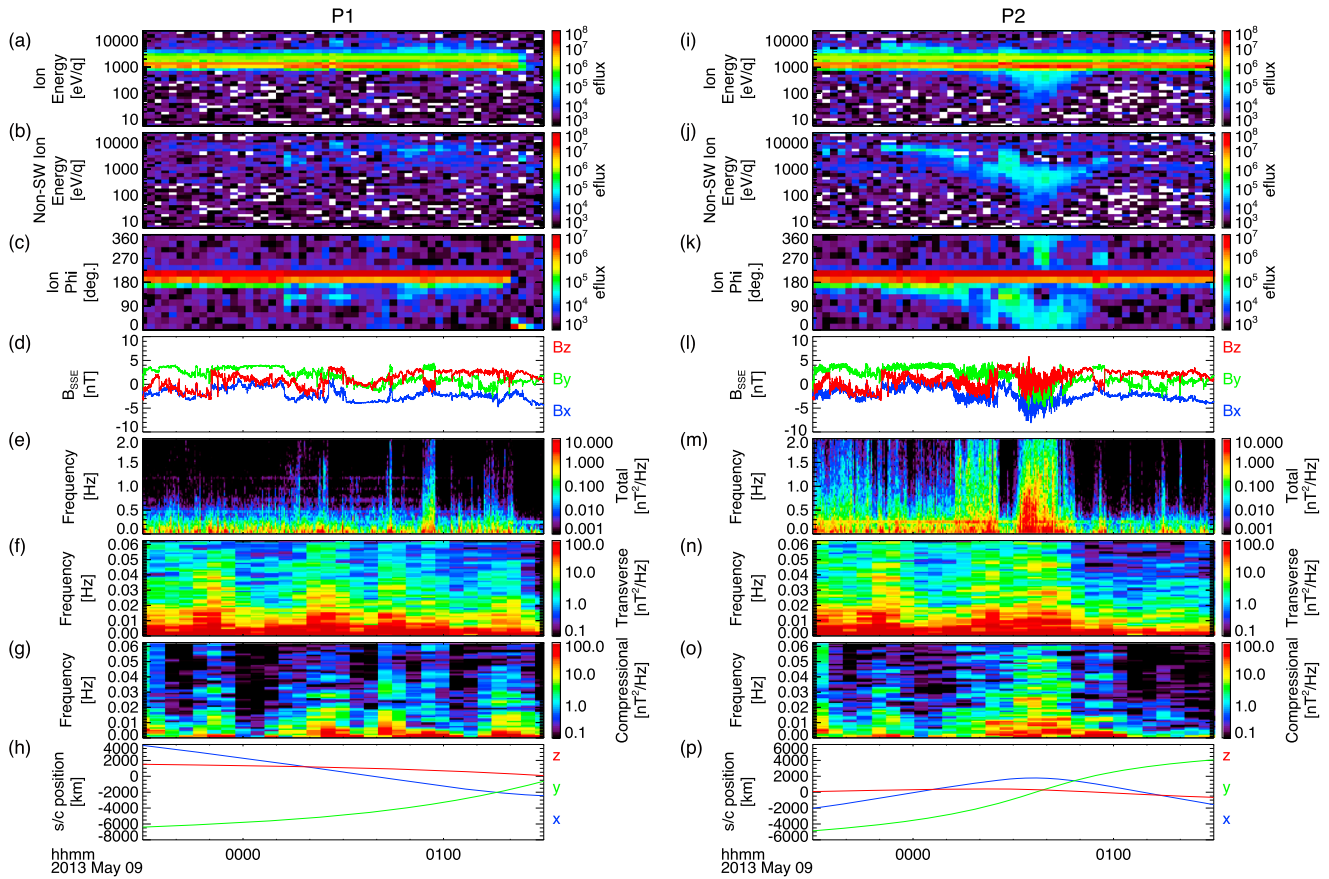


Figure 1. Time series data from ARTEMIS P1 and P2 in the solar wind on 8 and 9 May 2013, the same time interval as Figure 1 of *Harada et al.* [2014]. Ion energy spectra in units of $\text{eV}/\text{cm}^2/\text{s}/\text{str}/\text{eV}$ of (a) all ions and (b) nonsolar wind ions (see text for details); (c) ion azimuthal-angle spectra; (d) 4 Hz magnetic fields in the SSE coordinate system; magnetic field wave spectra for (e) 0–2 Hz total power, (f) 0–0.0625 Hz transverse power, and (g) 0–0.0625 Hz compressional power; and (h) SSE coordinates of the spacecraft position from P1; and (i–p) those from P2.

and locations of the two probes do not coincide during the vast majority of the orbits, and the spacecraft spend much more time observing the background plasma far from the Moon than close to the Moon given the highly eccentric ARTEMIS orbits. As shown in the following section, this simple subtraction produces very clean data which represent signals from lunar upstream particles and waves with only small background

3. Statistical Results

This section presents the main results of our statistical analysis. Medians of dual-probe quantities are plotted as a function of spacecraft position in the selenocentric solar ecliptic (SSE) or selenocentric solar electric (SSEI) coordinates. In the SSE system, the X axis points from the Moon toward the Sun, the Z axis is parallel to the upward normal to the Earth's ecliptic plane, and the Y axis completes the orthogonal coordinate set. The SSEI system has the same X axis as the SSE system, the Z axis is parallel to $\hat{\mathbf{x}} \times \mathbf{B}$, and the Y axis completes the orthogonal coordinate set. In the SSEI system, the motional electric field in the solar wind roughly points toward $+Z_{\text{SSEI}}$. Here the upstream magnetic field \mathbf{B} is derived from the mean of 8 s averaged magnetic field vectors detected by the two probes. When one probe is located in the wake (ion density $< 0.5 \text{ cm}^{-3}$ or spacecraft in the geometric shadow), we use the magnetic field at the other probe as the upstream field to avoid the field perturbation by wake current systems. In addition to maps derived from all the available data, we present the data divided into five cases according to the upstream IMF cone angle $\theta_{\text{IMF}} = \cos^{-1}(B_x/B)$ and clock angle $\phi_{\text{IMF}} = \tan^{-1}(B_y/B_z)$ in the SSE frame: IMF Parker spiral case with $(30^\circ < \theta_{\text{IMF}} < 60^\circ$ and $225^\circ < \phi_{\text{IMF}} < 315^\circ)$ or $(120^\circ < \theta_{\text{IMF}} < 150^\circ$ and $45^\circ < \phi_{\text{IMF}} < 135^\circ)$; IMF B_y case with $60^\circ < \theta_{\text{IMF}} < 120^\circ$ and $(45^\circ < \phi_{\text{IMF}} < 135^\circ$ or $225^\circ < \phi_{\text{IMF}} < 315^\circ)$; IMF B_x case with $0^\circ < \theta_{\text{IMF}} < 30^\circ$ or $150^\circ < \theta_{\text{IMF}} < 180^\circ$; IMF $+B_z$ case with $30^\circ < \theta_{\text{IMF}} < 150^\circ$ and $-45^\circ < \phi_{\text{IMF}} < 45^\circ$; and IMF $-B_z$ case with $30^\circ < \theta_{\text{IMF}} < 150^\circ$ and $135^\circ < \phi_{\text{IMF}} < 225^\circ$. The spatial bin size is $0.25R_L \times 0.25R_L$, and bins with less than three data points are not

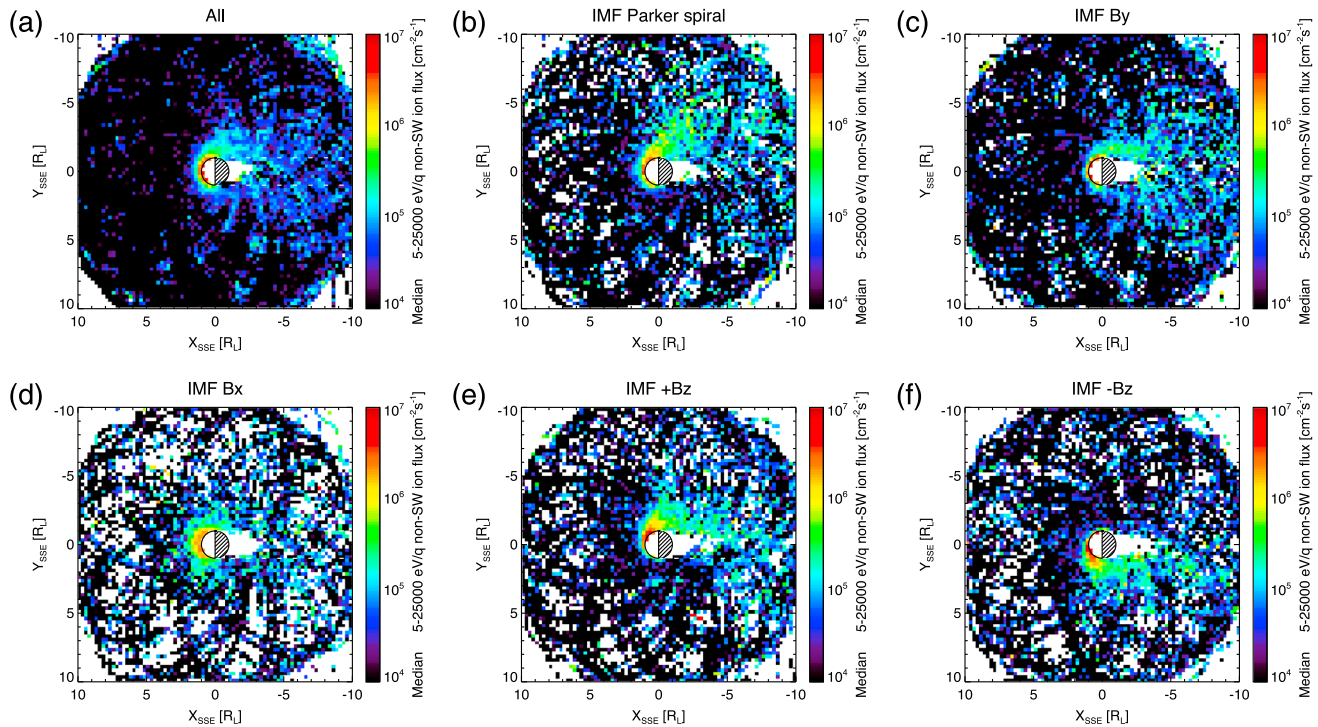


Figure 2. Spatial distributions of nonsolar wind ion flux in the SSE coordinates for different IMF directions: (a) all data, (b) IMF Parker spiral case, (c) IMF B_y case, (d) IMF B_x case, (e) IMF $+B_z$ case, and (f) IMF $-B_z$ case (see text for details).

plotted. The bins near the Moon typically contain ~ 20 –5000 data points, providing reasonably good statistics. The SSE distributions are shown in the X_{SSE} - Y_{SSE} plane with all Z_{SSE} range included in the plot. These maps effectively provide nearly ecliptic cuts because of the nearly ecliptic ARTEMIS orbits.

3.1. Moon-Related Ions

In order to extract Moon-related populations from the mixture of the solar wind and Moon-related ions, we mask the solar wind component based on the ion energy per charge E/q and angle: $0.4E_{SW}/e < E/q < 4E_{SW}/e$, where E_{SW}/e is the solar wind proton energy per charge and angles within 45° from the solar wind velocity direction. The rest is defined as nonsolar wind ions. Figure 1 shows a sample event that exhibits reflected and accelerated ion populations. Electron velocity distributions and higher-frequency waves in the same event are analyzed in detail by Harada *et al.* [2014]. It is seen that the nonsolar wind ions (Figures 1b and 1j) well represent the Moon-related ions that have different energies (Figures 1a and 1i) and/or different angles (Figures 1c and 1k) from the narrow, solar wind ion beam during this orbit. We observe ~ 100 –1000 eV/ q reflected ions on the dayside by P2 at 00:20–00:40 (Figure 1j) and accelerated ions with energies of a few keV/ q on the dawnside flank by P1 at 00:13, 00:20, and 00:50–01:00 (Figure 1b) and by P2 at 23:50–00:10 (Figure 1j). Note that the IMF B_z component is generally positive when the accelerated ions are observed on the dawnside, indicating that the spacecraft are located on the positive electric field hemisphere.

As our definition of the nonsolar wind ions is not applicable when the major solar wind component is absent, we only use ion observations outside the geometric shadow of the Moon. We note that this procedure also removes parts of reflected ions which are moderately accelerated to energies and angles similar to those of the solar wind ions. It is difficult to separate this minor component from the 1–2 orders of magnitude larger solar wind flux. When solar wind ions are hot, the derived “nonsolar wind” component includes the outer portion of the solar wind ion velocity distribution with fluxes above the one-count level. The nonsolar wind ions also contain backstreaming ions from the terrestrial bow shock when the Moon is located in the ion foreshock of the Earth. We find that most of these background populations can be removed by the dual-probe subtraction.

Figure 2a shows the X_{SSE} - Y_{SSE} distribution of the omnidirectional nonsolar wind ion flux with dual-probe subtraction. We observe enhanced fluxes of nonsolar wind ions in the vicinity of the Moon. These nonsolar wind ions can be associated with the Moon-related ions, which include ions of solar wind origin reflected by the

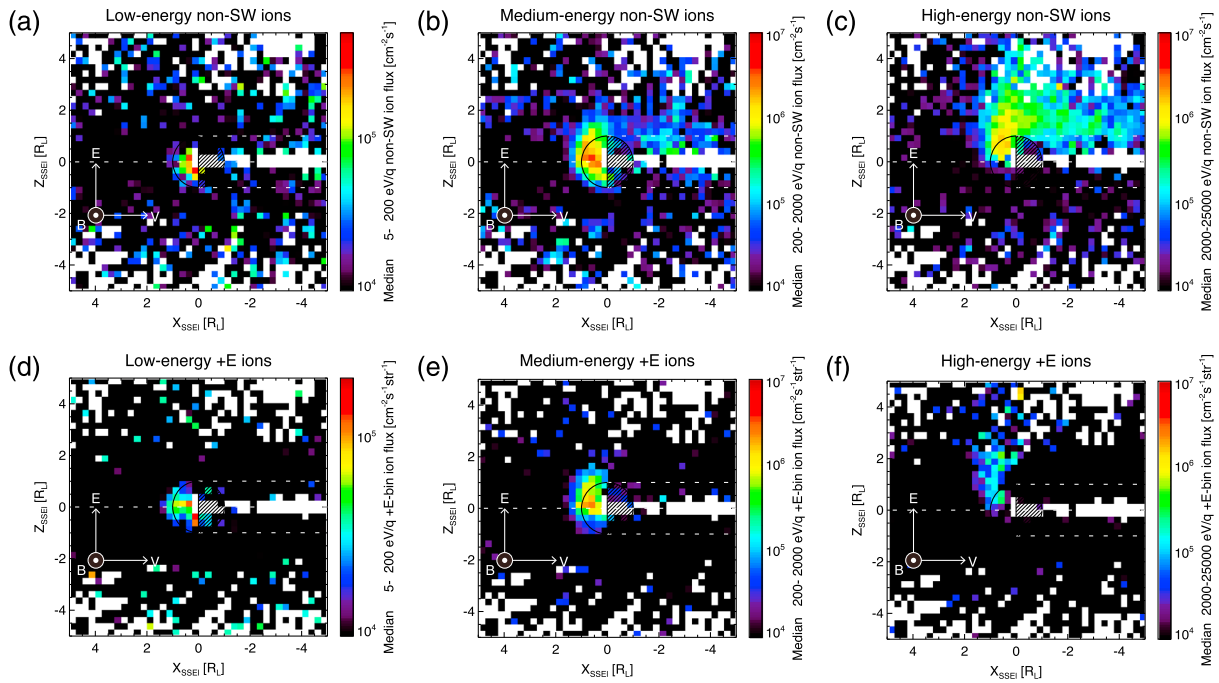


Figure 3. Spatial distributions in the selenocentric solar electric (SSEE) coordinates of (a) low-, (b) medium-, and (c) high-energy nonsolar wind ion flux and of (d) low-, (e) medium-, and (f) high-energy ion flux in a single solid-angle bin of the instrument which includes the motional electric field direction. Note that the color scales for low-energy ions are different from those for medium- and high-energy ions. Observations with IMF cone angles of $45^\circ - 135^\circ$ and $-1R_L < Y_{SSEE} < 1R_L$ are used.

crustal fields or from the lunar surface as well as heavy ions of lunar surface/exospheric origin. Hereafter we refer to the nonsolar wind ions enhanced around the Moon as Moon-related ions. Figures 2b–2f show the same maps but separated for different IMF directions. The spatial distributions of the Moon-related ions are well organized by IMF direction, reflecting the ion motion controlled by background magnetic and electric fields. In the nominal Parker spiral configuration (Figure 2b), we see an ion population extending from the dayside to dawnward and antisunward (toward the upper right corner), indicating that the Moon-related ions are convected downstream mainly perpendicularly to the background magnetic field. Such Moon-related ions conduct $\mathbf{E} \times \mathbf{B}$ drift toward the perpendicular direction in consequence of the motional electric field of the solar wind in the Moon rest frame, $\mathbf{E} = -\mathbf{V}_{SW} \times \mathbf{B}$, and spread in the parallel direction depending on their parallel velocities. The IMF B_y case also shows the perpendicular population, which is aligned with the X axis in the perpendicular IMF condition (Figure 2c). We find larger fluxes on the dawnside compared to the duskside, reasons of which will be discussed later. In the IMF B_x case, the enhanced flux region is more expanded toward upstream than the other cases (Figure 2d). This is consistent with weak motional electric fields and slow perpendicular drift in quasi-parallel IMF configurations, building up a column of reflected ions [Halekas et al., 2013]. Finally, the IMF $\pm B_z$ cases show clear dependence of the ion distributions on the motional electric field direction. In the northward IMF configuration (Figure 2e), Moon-related ions are distributed toward the dawnward electric field, while we observe flux enhancement on the duskside in the southward IMF configuration (Figure 2f).

The pickup acceleration process is shown in more detail in the electric field plane ($X_{SSEE}-Z_{SSEE}$) slices of low- (5–200 eV/q), medium- (200–2000 eV/q), and high-energy (2000–25,000 eV/q) ion distributions in quasi-perpendicular IMF configurations with $45^\circ < \theta_{IMF} < 135^\circ$ (Figure 3). We have confirmed that correction for the solar wind aberration does not change the results qualitatively (not shown). We observe low-energy Moon-related ions distributed mainly in $-Z_{SSEE}$ hemisphere (Figure 3a). The enhanced flux of low-energy ions in the antielectric field hemisphere can be attributed to reflected ions that are first launched to the $-Z_{SSEE}$ direction with medium energies of 200–2000 eV/q and then decelerated to low energies < 200 eV/q by the $+Z_{SSEE}$ electric field. Note that Figure 3a has a different color scale from those in Figures 3b and 3c. The low-energy ion flux is much smaller than the medium- and high-energy flux, indicating that the majority of the reflected ions have energies higher than 200 eV/q. The largest flux is found in the medium-energy range, which corresponds

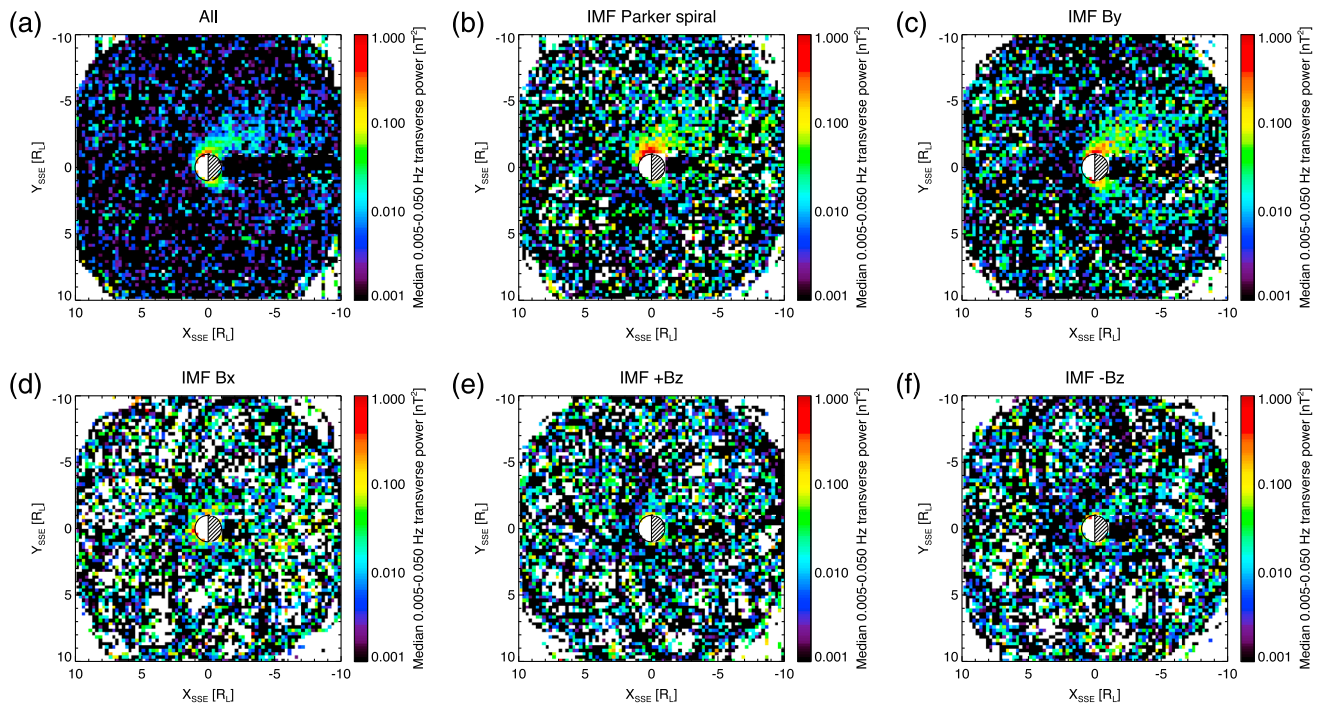


Figure 4. Spatial distributions of ~ 0.01 Hz transverse waves in the same format as Figure 2.

to the nominal energies of the reflected ions (Figure 3b). The high-energy ions are distributed predominantly in the $+Z_{SSEI}$ hemisphere, demonstrating the acceleration by the solar wind motional electric field (Figure 3c). The Moon-related ions are accelerated toward $+Z_{SSEI}$ from medium to high energies as they travel long distances along the electric field (Figures 3b and 3c). Figure 3c also shows that the high-energy Moon-related ions have two main pathways: one starting from the dayside and quickly bent toward antisunward and the other extending from the dayside to the $+Z_{SSEI}$ direction in a nearly straight line. The former presumably corresponds to reflected protons that are more easily deflected by magnetic force, while the latter represents heavier pickup ions of lunar origin with much larger gyroradii. In some cases the reflected protons have gyroradii close to the lunar radius, leading to proton entry deep into the lunar wake [Nishino *et al.*, 2009]. Meanwhile, gyroradii of the heavy pickup ions are much larger than the lunar radius, enabling acceleration to very high energies in giant cycloid trajectories [Yokota and Saito, 2005] (see also the $+Z_{SSEI}$ -extended population in Figure 3f and the following paragraph).

Figures 3d–3f show SSEI distributions of ion flux in a single solid-angle bin of the instrument along the solar wind motional electric field. As the heavy pickup ions have essentially zero initial velocities, their velocities are aligned with the electric field direction until magnetic force becomes effective. On the other hand, reflected ions have a wide variety of initial velocities [Futaana *et al.*, 2003; Saito *et al.*, 2010]. Only a small portion of the reflected ions contribute to the electric-field-aligned flux in a single solid-angle bin. The electric-field-aligned ion flux exhibits different distributions from the omnidirectional flux. We note that the low-energy electric-field-aligned ions are found on the dayside mainly in the $+Z_{SSEI}$ hemisphere (Figure 3d), while the omnidirectional flux shows the opposite trend toward the $-Z_{SSEI}$ hemisphere (Figure 3a). This low-energy population traveling along the electric field is consistent with ions of lunar origin in an early phase of pickup acceleration. The medium- and high-energy electric-field-aligned ion fluxes display pickup acceleration of both reflected and lunar origin ions along the electric field (Figures 3e and 3f). Note that a typical motional electric field of 1 mV/m can cause \sim keV acceleration over a $1R_L$ distance. The high-energy pickup ion population extends over $Z_{SSEI} > 2R_L$, corresponding to well-accelerated heavy ions of lunar origin.

3.2. Approximately 0.01 Hz Magnetic Field Fluctuations

Next we look at low-frequency magnetic field fluctuations observed around the Moon. We apply the fast Fourier transform (FFT) to 8 s averaged magnetic field data sliding a 1024 s Hamming window by 256 s. The obtained wave spectra for the transverse and compressional components during the sample event are shown

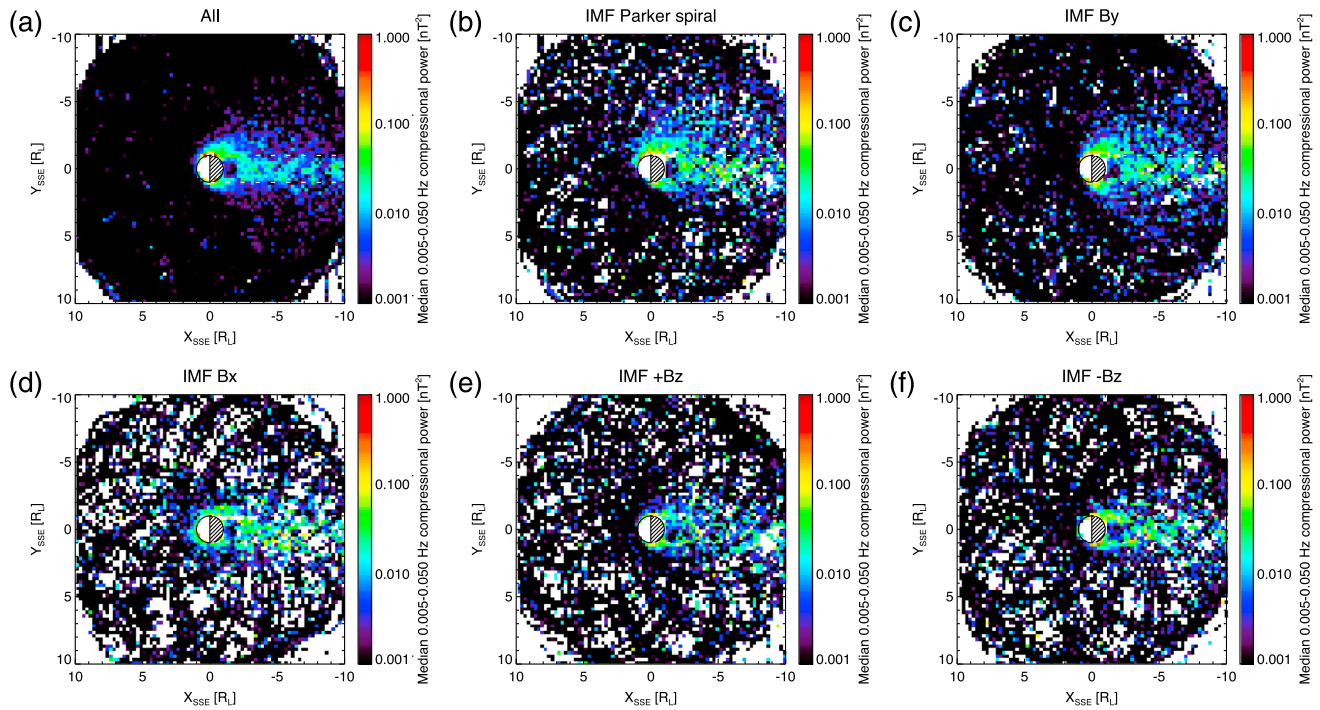


Figure 5. Spatial distributions of ~ 0.01 Hz compressional waves in the same format as Figure 2.

in Figures 1f, 1g, 1n, and 1o. The enhanced fluctuations of both the transverse and compressional components are observed by P2 on the dayside at 00:30–00:50 (Figures 1n and 1o) and by P1 around the wake boundary at 01:10–01:30 (Figures 1f and 1g). We note that the observed magnetic field fluctuations do not necessarily exhibit clear narrowband features in contrast to the previous work [Nakagawa *et al.*, 2012; Halekas *et al.*, 2013].

Figures 4 and 5 show X_{SSE} - Y_{SSE} distributions of the 0.005–0.05 Hz transverse and compressional components, respectively. To eliminate strong broadband spectra caused by artificial/natural sharp discontinuities, we reject the 1024 s interval magnetic field data if at least one of the three components jumps over 4 nT per 8 s or the magnetic field vector changes its direction over 60° per 8 s at some point within that interval. The dual-probe subtraction of the integrated transverse power results in a moderate success in canceling Alfvénic fluctuations embedded in the background solar wind; i.e., the lunar signals with warm colors can be identified, though we see the green color background noise in Figure 4. The spatial pattern of the wave distributions changes according to the IMF direction. In the IMF Parker spiral and B_y cases (Figures 4b and 4c), the transverse waves are distributed over the flanks starting from the tangential point of the field line and the Moon’s dayside. Higher levels of transverse-wave activity are observed on the dawnside than on the duskside. We see less clear enhancement of transverse waves near the Moon in the IMF B_x configuration (Figure 4d). In the IMF $\pm B_z$ cases (Figures 4e and 4f), no significant enhancement of Moon-related transverse waves is found except in the very low-altitude terminator regions. The transverse wave activity is generally low in the lunar wake for all IMF configurations.

The compressional component shows different distributions from the transverse component, particularly in the lunar wake region (Figure 5). We observe compressional waves distributed from the limb into the central wake and well extended toward the downwake (Figure 5a). We note that this compressional fluctuation in and around the wake may include the spatial structures of magnetic fields generated by complex current systems around the Moon [e.g., Fatemi *et al.*, 2013, 2014]. The spatial pattern of the compressional component outside the lunar wake is organized by the IMF direction in a similar fashion to the transverse component. In the IMF Parker spiral and B_y cases (Figures 5b and 5c), the enhanced waves are observed over the flanks starting from the field-line tangential point with small dawn-dusk asymmetry. We see the slightly enhanced power on the dayside in the IMF B_x case (Figure 5d). The compressional power enhancement in the upstream region is limited to low altitudes in the IMF $\pm B_z$ configurations (Figures 5e and 5f).

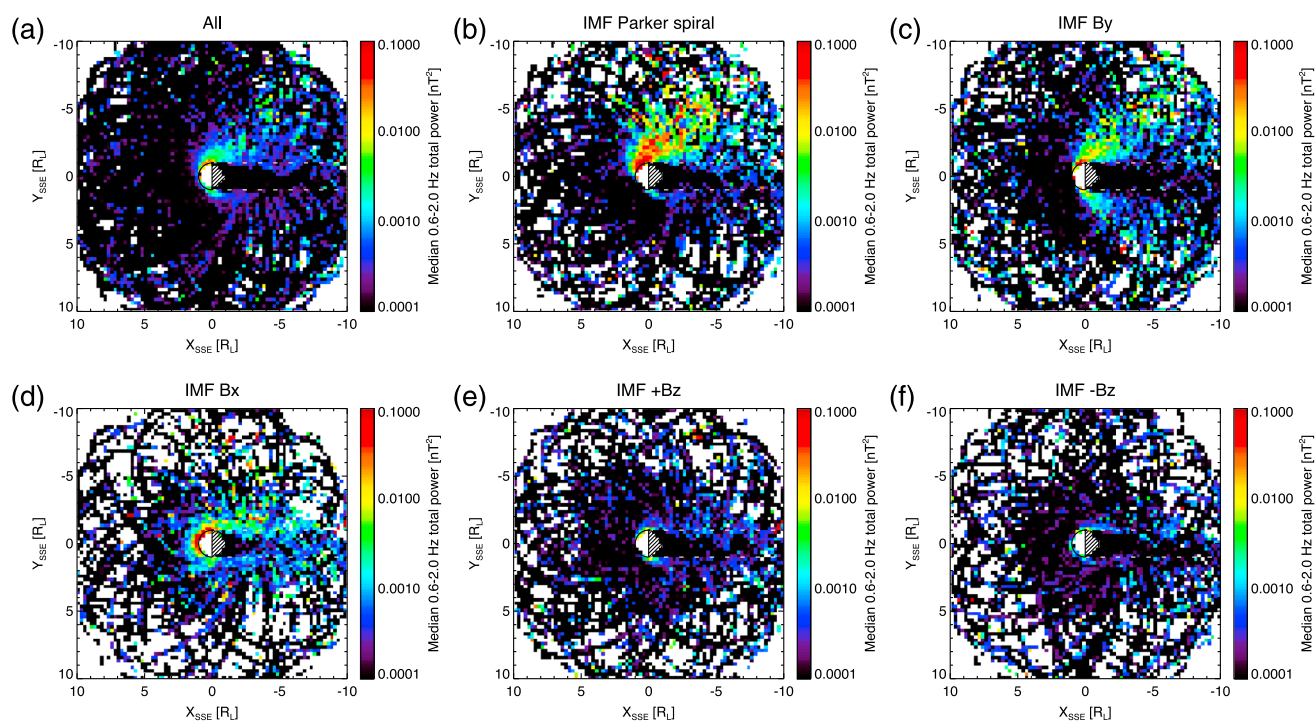


Figure 6. Spatial distributions of ~ 1 Hz waves in the same format as Figure 2.

3.3. Approximately 1 Hz Whistlers

We move up in frequency to ~ 1 Hz waves. Here we apply FFT to 4 Hz magnetic field data sliding a 32 s Hamming window by 8 s. Figures 1e and 1m show the obtained magnetic field wave spectra for the sample event. The strong broadband fluctuations are observed by P2 on the dayside at 00:10–00:25 and 00:30–00:45 (Figure 1m).

Figure 6 shows X_{SSE} - Y_{SSE} distributions of total wave power integrated over 0.6–2 Hz with dual-probe subtraction. The lower frequency limit 0.6 Hz is chosen so that we can exclude spin tones up to the second harmonics ~ 0.5 Hz. We note that both broadband fluctuations and narrowband waves contribute to the wave power in this frequency range. In this paper, we loosely use the term “ ~ 1 Hz waves” to refer to enhanced magnetic field fluctuations with frequencies of 0.6–2 Hz regardless of their spectral characteristics. Distributions of the transverse and compressional components in this frequency range exhibit essentially the same pattern with different magnitudes (not shown). In the IMF Parker spiral and B_y cases (Figures 6b and 6c), the wave distributions are extended along field lines from the Moon and its wake. The ~ 1 Hz waves are distributed from the dayside field line tangential point in a similar way to the lower frequency waves. We observe distinctly strong wave emissions on the dawnside in the IMF Parker spiral case (Figure 6b) and on the dayside in the IMF B_x case (Figure 6d). In the IMF $\pm B_z$ configurations (Figures 6e and 6f), only weak emissions are seen in the low-altitude terminator regions. No significant wave activity is found inside the lunar wake.

3.4. Mach Number Dependence of Low-Frequency Waves

The morphology of the ~ 0.01 Hz and ~ 1 Hz waves is organized not only by the IMF direction but also by the upstream Mach numbers. Figures 7a–7c show the X_{SSE} - Y_{SSE} distributions of the ~ 0.01 Hz transverse, ~ 0.01 Hz compressional, and ~ 1 Hz total power in the IMF Parker spiral configuration for low Alfvén Mach numbers ($M_A < 6$), while Figures 7d–7f show those for high Mach numbers ($M_A > 6$). All the three types of waves are more extended upstream in the low Mach number condition. This is consistent with upstream propagating waves with higher ratios of the wave group velocities relative to the flow velocity. In low Mach number conditions, these waves can travel further from the Moon before they are convected downstream, and their propagation cones become wider. Also, we observe larger cone angles for the ~ 1 Hz waves compared to those of the ~ 0.01 Hz waves as expected from higher group velocities of ~ 1 Hz whistlers than lower frequency MHD wave group velocities.

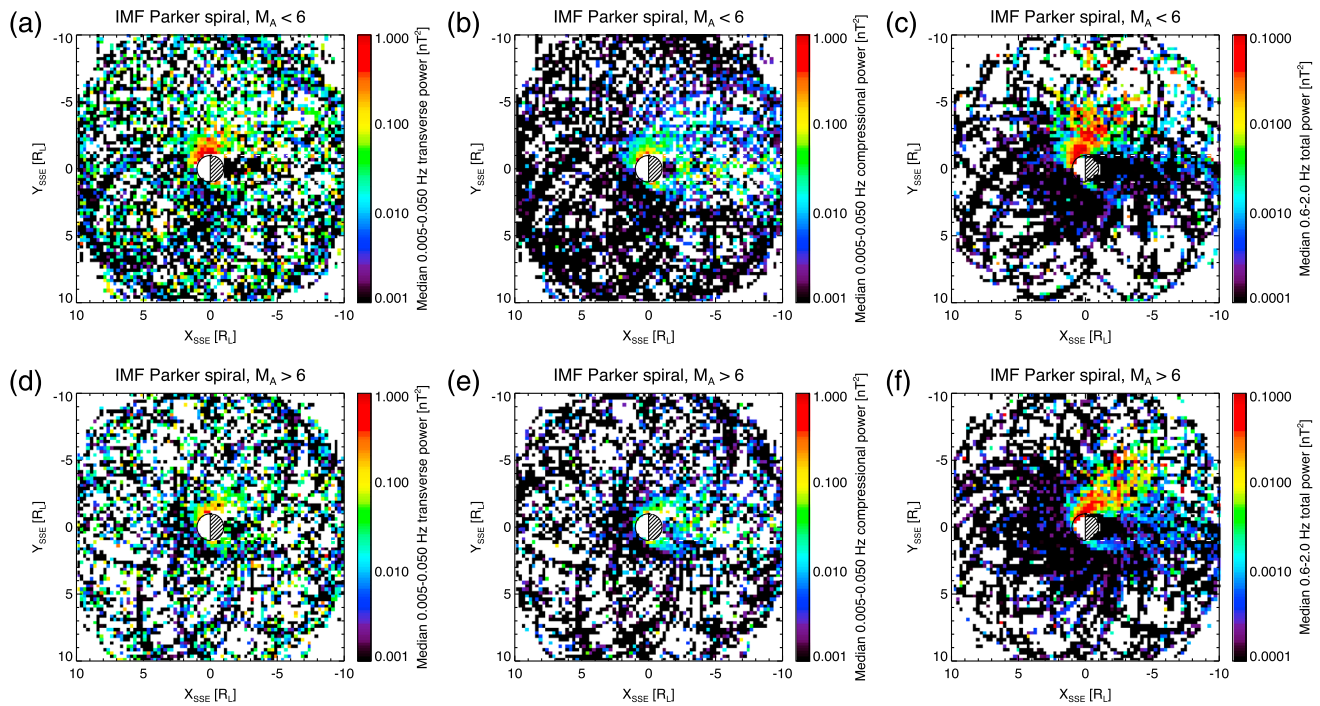


Figure 7. Spatial distributions of (a) transverse and (b) compressional components of ~ 0.01 Hz waves, (c) ~ 1 Hz waves in low Mach number conditions, and (d–f) those in high Mach number conditions for IMF Parker spiral cases.

3.5. Electron Loss Cones and ~ 100 Hz Whistlers

Occurrence of modified electron velocity distributions and higher-frequency whistlers is primarily determined by magnetic connection to the Moon. Hereafter the field line connection to the Moon is estimated from the straight-line tracing of the magnetic field measured at the spacecraft under the assumption of a spherical Moon. Figure 8 shows X_{SSE} - Y_{SSE} distributions of maximum electron anisotropy, maximum whistler growth rates computed from the measured electron distribution, and magnetic field wave intensity integrated over 10–200 Hz. The v_{\parallel} -dependent electron anisotropy, $A(v_{\parallel}) = \int (v_{\parallel} \partial f / \partial v_{\perp} - v_{\perp} \partial f / \partial v_{\parallel}) v_{\perp}^2 / v_{\parallel} dv_{\perp} / \int 2f v_{\perp} dv_{\perp}$, represents the temperature anisotropy caused by the combination of the surface absorption and magnetic/electrostatic reflection of electrons [Kennel and Petschek, 1966; Santolik et al., 2011]. It can be used as a measure of loss cone distributions related to the whistler mode growth rate $\gamma(v_{\parallel}) / \omega_{ce} = \pi(1 - \omega / \omega_{ce})^2 \eta(v_{\parallel}) [A(v_{\parallel}) - 1 / (\omega_{ce} / \omega - 1)]$, where $\eta(v_{\parallel})$ is the fraction of resonant electrons $\eta(v_{\parallel}) = 2\pi v_{\parallel} \int f(v_{\parallel}, v_{\perp}) v_{\perp} dv_{\perp} / N_e$. These quantities are derived in the same manner as Harada et al. [2014], and dual-probe subtraction is applied when plotting them. We observe enhancement of the three quantities only when magnetic field lines are connected to the Moon (Figures 8a–8c) and no enhancement is seen during unconnected intervals (Figures 8d–8f). The distributions of the computed local growth rates (Figure 8b) and detected whistlers (Figure 8c) show consistent features, suggesting a direct link between the electron velocity distributions and higher-frequency whistlers. All the three quantities exhibit clear day-night asymmetry. Meanwhile, the electron anisotropy shows additional dawn-dusk asymmetry. This dawn-dusk asymmetry is not seen in the growth rate and wave power distributions. We will discuss the day-night and dawn-dusk asymmetry in the following section.

3.6. Approximately 1 kHz Electrostatic Waves

Figure 9 shows X_{SSE} - Y_{SSE} distributions of electric field wave intensity integrated over 300–8000 Hz with dual-probe subtraction. As was done by Harada et al. [2014], we reject wave spectra if the 10–1000 Hz integrated power exceeds 10^{-9} (V/m)² to exclude contamination from the nongeophysical periodic low-frequency bursts. The high-frequency electrostatic waves are observed when magnetic field lines are connected to the Moon regardless of solar zenith angles (Figure 9a). Such broadband electrostatic emission is observed simultaneously with field-aligned electron beams upcoming from the Moon [Harada et al., 2014], and the upward electron beams are commonly observed on both the dayside and nightside [Halekas et al., 2002, 2012b]. Figures 9b and 9c show electric field wave distributions when magnetically connected to the

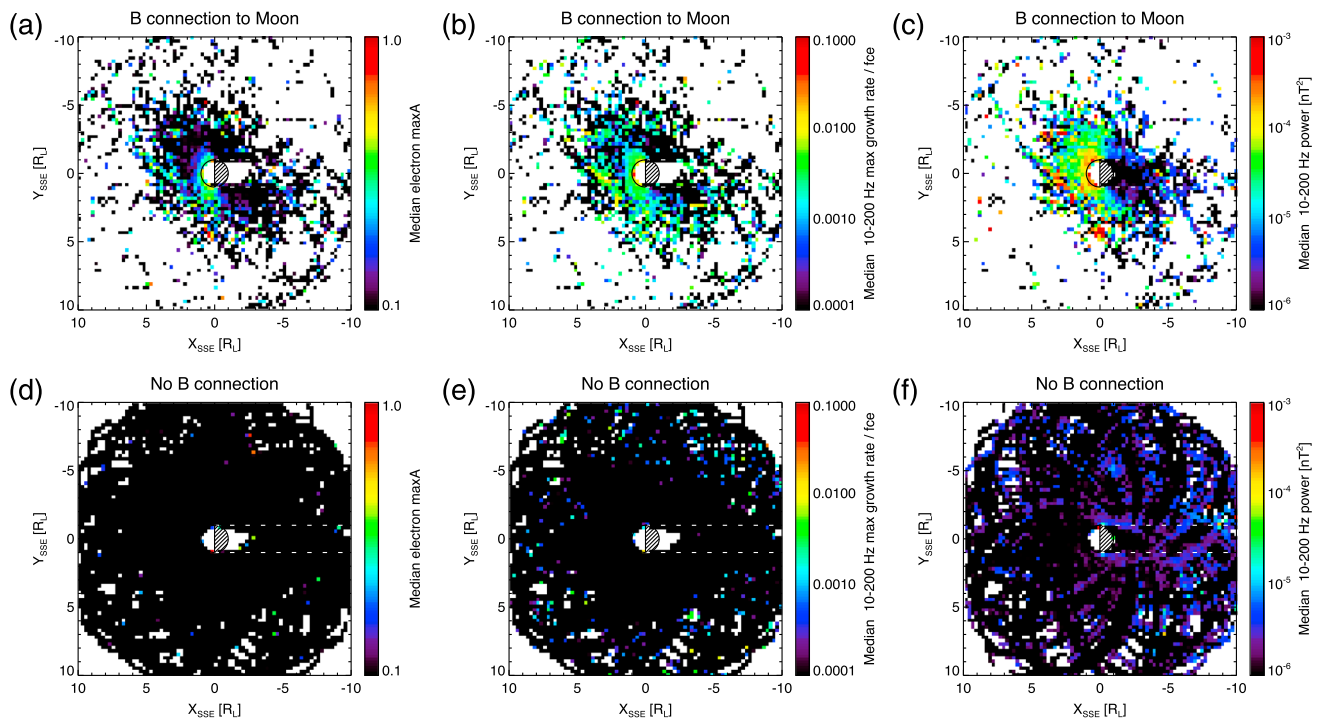


Figure 8. Spatial distributions of (a) maximum electron anisotropy, (b) maximum growth rate, and (c) ~ 100 Hz whistler waves when magnetic field lines are connected to the Moon and (d–e) those during unconnected intervals.

geometric shadow and when field lines are not connected to the Moon inside the geometric shadow, respectively. These wake-related electric field waves can be associated with electron velocity distributions modified either by the ambipolar potential drop or by Type-II ion entry [Futaana et al., 2001; Nishino et al., 2010, 2013; Halekas et al., 2011; Tao et al., 2012]. When field lines are not connected to the Moon nor to the lunar wake, no significant electrostatic emission is observed outside the wake (Figure 9d).

4. Discussion

In this section, we discuss previously suggested properties and newly found features of the foremoon, based on the statistical results presented in the previous section.

The Moon-related ions in different IMF configurations behave mostly as expected from pickup acceleration of reflected ions and heavy ions of lunar origin. The Moon-related ion distribution in the Parker spiral case (Figure 2c) shows very similar properties to simulation results with the Parker spiral IMF [Holmström et al., 2010; Fatemi et al., 2014]. The dayside accumulation of reflected ions in the parallel IMF case (Figure 2d) was proposed and simulated to account for the generation of the coherent, low-frequency magnetic field waves observed in the quasi-parallel IMF [Halekas et al., 2013]. Figure 2d demonstrates that the backstreaming ions are accumulated above the entire lunar dayside, which could provide with significant energy source for wave growth in this special IMF configuration. Perhaps the stronger flux on the dawnside in the IMF B_y case (Figure 2c) appears an unexpected feature, and this will be discussed later. The low-energy and high-energy heavy pickup ions have been studied from observations at ~ 100 km altitudes [Yokota et al., 2009] and from fewer observations at high altitudes [Halekas et al., 2012a], respectively. We now confirm the continuously extended pickup ion population from the low-altitude lunar dayside all the way up to at least several lunar radii altitudes along the solar wind motional electric field (Figures 3d–3f).

Next we discuss low-frequency (~ 0.01 Hz and ~ 1 Hz) wave distributions shown in Figures 4–7. The outward expansion of the magnetic field fluctuations in the region magnetically connected to the lunar wake (also referred to as the forewake in the literature) was observed first by Explorer 35 [Ness and Schatten, 1969] and later by Wind [Farrell et al., 1996] and Geotail [Nakagawa et al., 2003]. The dayside magnetic field fluctuations have been observed by a number of low-altitude spacecraft [Lin et al., 1998; Halekas et al., 2006, 2008; Nakagawa et al., 2011, 2012; Tsugawa et al., 2011, 2012] and also by ARTEMIS [Halekas et al., 2012c, 2013].

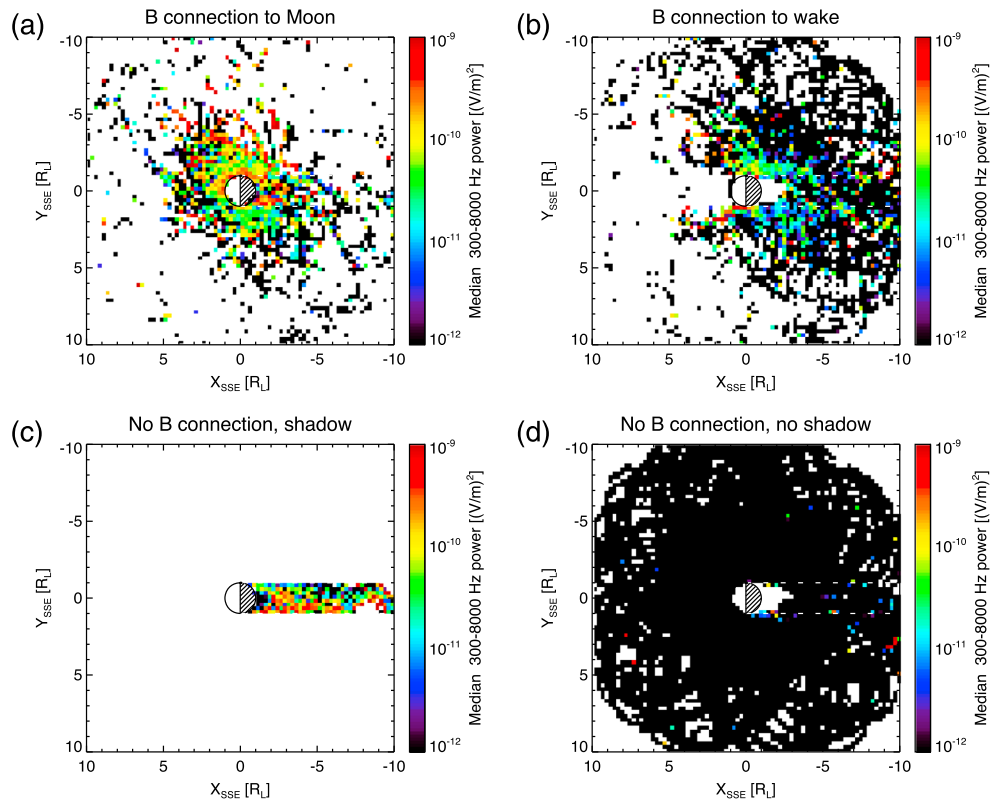


Figure 9. Spatial distributions of high-frequency electrostatic waves when (a) field lines are connected to the Moon, (b) field lines are connected to the geometric shadow, (c) field lines are not connected to the Moon but the spacecraft are located in the geometric shadow, and (d) field lines are not connected to the Moon nor to the geometric shadow and the spacecraft are outside the geometric shadow.

These forewake and dayside waves have been reported and discussed separately perhaps because they were implicitly assumed to be different phenomena with different origins. However, the large-scale distributions of the ~ 0.01 Hz and ~ 1 Hz waves exhibit continuous wave distributions from the dayside to the forewake (Figures 4b, 4c, 5b, 5c, 6b, and 6c). These statistical distributions suggest that careful examination is needed to conclude unambiguously that the observed forewake waves originate from the wake, because part of these waves could be generated on the lunar dayside or near the terminator and then convected downstream to the forewake by the solar wind. We note that a field line which is now connected to the geometric shadow used to be connected to the Moon as well, unless the field line changes its direction rapidly while it is convected downstream. Along those lines, the Mach number control of wave propagation cones (also known as Mach cones) is expected naturally, and Figure 7 observationally demonstrates such effects on lunar upstream waves.

The magnetic-connection control of the electron-related waves (Figures 8 and 9) is consistent with the previous observations [Halekas et al., 2012c; Harada et al., 2014]. The electrostatic waves in the lunar wake are widely distributed from the near wake to the distant wake (Figure 9c), indicating the common presence of electrostatic emission all over the wake which is inferred from the individual event studies [Farrell et al., 1997; Nishino et al., 2010; Tao et al., 2012] and was predicted by simulations [Farrell et al., 1998]. The day-night asymmetry in Figures 8a–8c is a new feature revealed by the statistical results. This asymmetry can be associated with two effects: negative surface potentials on the nightside and electron density decrease in the wake. As the nightside lunar surface is charged negatively owing to the lack of the photoelectron current, more electrons are reflected on the nightside. Electron loss cones are more filled by these electrically reflected populations, leading to smaller anisotropy (Figure 8a). Besides, the electron density drops in the wake, resulting in the higher magnetic energy per particle $E_c = B^2/2\mu_0 N_e$ (equivalently lower f_{pe}/f_{ce}) and smaller fraction of resonant electrons [Kennel and Petschek, 1966]. The combination of these two effects could lead to the lower growth rates (Figure 8b) and weaker whistler emission (Figure 8c) on the nightside compared to the dayside.

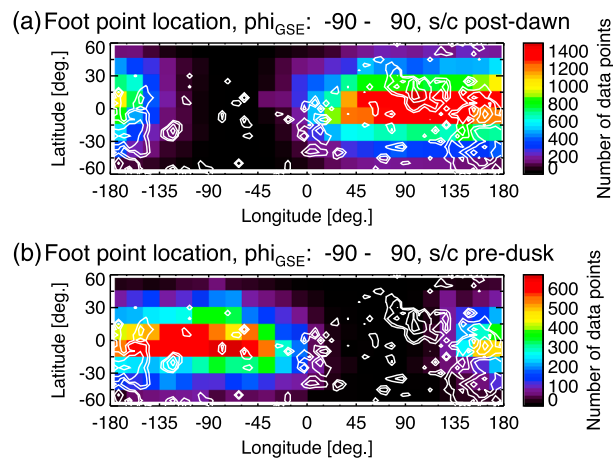


Figure 10. Surface distributions of field line foot points when the spacecraft are located on (a) the postdawn ($-90^\circ < \phi_{SSE} < -45^\circ$) and (b) the predusk ($45^\circ < \phi_{SSE} < 90^\circ$) section of the Moon, where ϕ_{SSE} is the azimuthal angle of the spacecraft position in the SSE coordinates. The white contours denote the surface strength of the crustal magnetic fields derived from Lunar Prospector magnetometer/electron reflectometer measurements with lines for 10 nT, 20 nT, 50 nT, 100 nT, and 200 nT [Mitchell et al., 2008].

and the electron anisotropy is reduced on the dawnside (Figures 2c and 8a). Previous observations have shown that the occurrence and intensity of the low-frequency waves and field disturbances are correlated with lunar magnetic anomalies [Russell and Lichtenstein, 1975; Halekas et al., 2006; Tsugawa et al., 2011, 2012; Nakagawa et al., 2012], which are consistent with the stronger wave power on the dawnside (Figures 4c, 5c, and 6c).

The clear dawn-dusk asymmetry seen in the electron anisotropy distribution (Figure 8a) does not appear in the growth rate distribution computed from the same electron velocity distributions (Figure 8b). This means that the smaller anisotropy must be compensated by larger fraction of resonant electrons on the dawnside, because the growth rate depends on the product of the electron anisotropy and fraction of resonant electrons. The asymmetric distribution of resonant electrons can be attributed to the blockage by the Moon of suprathermal electrons coming from the Sun. In the nominal Parker spiral configuration, dawnside field lines are located between the Sun and Moon, and all electrons exiting from the Sun are incident on the dawnside of the Moon. On the other hand, duskside field lines are more likely located behind the Moon, leading to blockage of antisunward electrons by the Moon. As a result, more suprathermal electrons are incident on and reflected from the Moon's dawnside compared to the duskside. The opposite asymmetry of the anisotropy and fraction of resonant electrons results in nearly symmetric distributions of the computed growth rate and observed whistlers (Figures 8b and 8c).

It is proposed that reflected ions can provide free energy sources for the ~ 0.01 Hz and ~ 1 Hz waves [Nakagawa et al., 2011, 2012; Tsugawa et al., 2011, 2012; Halekas et al., 2013]. The Moon-related ions do exhibit similar global distributions to the low-frequency wave distributions. For example, the ion population extending from the dayside to dawnward and antisunward in the Parker spiral case (Figure 2b) coincides with enhanced ~ 0.01 Hz transverse waves (Figure 4b) and ~ 1 Hz waves (Figure 6b). The distributions of the Moon-related ions and ~ 1 Hz waves are strikingly similar in the IMF B_x case (Figures 2d and 4d). However, we also find significant difference between the ion and wave distributions. We observe plenty of Moon-related ions that are picked up by the solar wind and gyrate around the Moon in the IMF $\pm B_z$ cases (Figures 2e and 2f), but almost no waves are observed in the same regions (Figures 4e, 4f, 5e, 5f, 6e, and 6f). This indicates that the presence of Moon-related ions is not a sufficient condition for detectable wave occurrence.

5. Conclusions

We have conducted comprehensive statistics using ARTEMIS data to investigate the global distributions of lunar influence on the surrounding solar wind plasma. In contrast to the classical model of the Moon-solar wind interaction, which implies no perturbation in the upstream plasma, the ARTEMIS observations exhibit

Dawn-dusk asymmetry is found in the distributions of the Moon-related ions (Figure 2c), ~ 0.01 Hz waves (Figures 4c and 5c), ~ 1 Hz waves (Figure 6c), and electron anisotropy (Figure 8a). The Moon-related ions and low-frequency waves are enhanced on the dawnside, while the electron anisotropy is suppressed on the dawnside. This can be explained by biased sampling of crustal magnetic fields. Figure 10 shows field line foot point distributions on the lunar surface for different spacecraft locations on the postdawn and predusk. The foot points are not uniformly distributed in longitude because the limited range of lunar phase is used for our statistics. Consequently, the dawnside probes are more likely connected to strongly magnetized regions compared to the duskside probes. As the stronger magnetic fields reflect more ions and electrons, the Moon-related ion flux is enhanced,

the well-extended forenoon, where a wide variety of Moon-related waves and particles are present. The observed properties of the large-scale forenoon morphology are generally consistent with what is expected from the previous observations and simulations, but they also reveal new aspects of the forenoon.

Moon-related ion populations, which consist of reflected solar wind ions and heavy ions of lunar origin, are first accelerated toward the motional electric field direction from the Moon's dayside. When the IMF is nearly perpendicular to the solar wind velocity, the reflected protons quickly gyrate around the magnetic field with gyroradii which often happen to be comparable to the lunar radius. The heavy ions, on the other hand, have much larger gyroradii and travel in huge cycloid trajectories, forming long populations extending from the Moon's dayside. In quasi-parallel IMF conditions, reflected ions can travel further upstream in weak motional electric fields. In this case, we observe a cloud of reflected ions that is more expanded upstream compared to the quasi-perpendicular IMF case.

Spatial distributions of both transverse and compressional components of ULF waves with frequencies ~ 0.01 Hz are controlled by the IMF direction. Strong magnetic field fluctuations are observed in the upstream region behind the tangential field line. The transverse component exhibits strong dawn-dusk asymmetry near the terminator and becomes very weak in the lunar wake. Meanwhile, the compressional fluctuations have less pronounced dawn-dusk asymmetry and expand into the lunar wake. The different distributions of the two components suggest different sources and/or different propagation properties. Maps of ~ 1 Hz waves also show clear dependence on the IMF direction and pronounced dawn-dusk asymmetry. The ~ 0.01 Hz and ~ 1 Hz waves are continuously distributed from the dayside over the terminator to the forewake, suggesting possible connection between the dayside and forewake waves. The morphology of these low-frequency waves is sorted by another parameter: Mach numbers. We observe enhanced wave intensity more upstream in low Alfvén Mach number cases. The wave distributions in high Alfvén Mach number conditions display narrower propagation cones, indicating that waves are convected downstream faster. Although these low-frequency waves partially coincide with the Moon-related ions, only ions are observed in some conditions.

Electron anisotropy, linear growth rates of whistler mode waves computed from the measured electron velocity distributions, and detected power of higher-frequency ~ 100 Hz whistlers are all enhanced on the field lines connected to the Moon. Clear day-night asymmetry is found for these quantities, which are larger on the dayside and smaller on the nightside. This asymmetry can be explained by large negative potentials on the nightside lunar surface, which reflects more electrons and reduces the electron anisotropy and wave growth. We observe pronounced dawn-dusk asymmetry in the electron anisotropy but not in the computed growth rate and observed whistler intensity. The dawn-dusk asymmetry of electron anisotropy is presumably due to biased magnetic field strengths at field line foot points; i.e., dawnside spacecraft are more likely connected to stronger crustal fields when the Moon is located in the solar wind. This asymmetry could be compensated by larger incoming flux of suprathermal electrons on the dawnside owing to the lunar blockage of antisunward electrons on the duskside. The smaller anisotropy and larger fraction of resonant electrons on the dawnside result in nearly dawn-dusk-symmetric distributions of the computed whistler growth rates and observed whistler emissions.

Strong high-frequency electrostatic waves are observed on the field lines connected to the Moon or lunar wake and when the spacecraft are located in the wake. The electrostatic emission with frequencies lower than the electron plasma frequency can be driven by outward traveling electron beams from both the dayside and nightside lunar surfaces and by electron velocity distributions modified by the wake potential.

The statistical results presented in this paper have illustrated global characteristics of lunar upstream particles and waves as well as how the upstream parameters control them. Although these results have important implications for generation and propagation of the lunar upstream particles and waves, detailed physical processes responsible for the observed signatures are not yet uncovered. Further studies which focus on each category of lunar upstream phenomena would be necessary to fully understand this complex upstream region where multiple particle populations and wave modes may be interconnected.

References

- Anderson, K. A., R. P. Lin, R. E. McGuire, and J. E. McCoy (1975), Measurement of lunar and planetary magnetic fields by reflection of low energy electrons, *Space Sci. Instrum.*, *1*, 439–470.
- Angelopoulos, V. (2011), The ARTEMIS mission, *Space Sci. Rev.*, *165*(1–4), 3–25, doi:10.1007/s11214-010-9687-2.
- Auster, H. U., et al. (2008), The THEMIS fluxgate magnetometer, *Space Sci. Rev.*, *141*(1–4), 235–264, doi:10.1007/s11214-008-9365-9.

Acknowledgments

The authors acknowledge support through NASA contract NAS5-02099, as well as V. Angelopoulos for the use of data from the THEMIS mission; J.W. Bonnell and F.S. Mozer for the use of EFI data; A. Roux and O. LeContel for the use of SCM data; and K.H. Glassmeier, U. Auster, and W. Baumjohann for the use of FGM data, provided under the lead of the Technical University of Braunschweig (Germany) and with financial support from both the German Ministry for the Economy and Technology and the German Center for Aviation and Space (DLR) under contract 50 OC 0302. The authors gratefully acknowledge support from the NASA LASER program, grant NNX13AJ97G. ARTEMIS data are publicly available at <http://artemis.ssl.berkeley.edu>.

Yuming Wang thanks three anonymous reviewers for their assistance in evaluating this paper.

- Bale, S., C. Owen, J. Bougeret, K. Goetz, P. Kellogg, R. Lepping, R. Manning, and S. Monson (1997), Evidence of currents and unstable particle distributions in an extended region around the lunar plasma wake, *Geophys. Res. Lett.*, *24*(11), 1427–1430, doi:10.1029/97GL01193.
- Benson, J., J. W. Freeman, and H. K. Hills (1975), The lunar terminator ionosphere, in *Proc. 6th Lunar Sci. Conf., Houston, Tex.*, pp. 3013–3021, Pergamon Press, New York, March 17–21.
- Bonnell, J. W., F. S. Mozer, G. T. Delory, A. J. Hull, R. E. Ergun, C. M. Cully, V. Angelopoulos, and P. R. Harvey (2008), The Electric Field Instrument (EFI) for THEMIS, *Space Sci. Rev.*, *141*(1–4), 303–341, doi:10.1007/s11214-008-9469-2.
- Coates, A. J., and G. H. Jones (2009), Plasma environment of Jupiter family comets, *Planet. Space Sci.*, *57*(10), 1175–1191, doi:10.1016/j.pss.2009.04.009.
- Colburn, D. S., R. G. Currie, J. D. Mihalov, and C. P. Sonett (1967), Diamagnetic solar-wind cavity discovered behind Moon, *Science*, *158*, 1040–1042, doi:10.1126/science.158.3804.1040.
- Farrell, W., R. Fitzenreiter, C. Owen, J. Byrnes, R. Lepping, K. Ogilvie, and F. Neubauer (1996), Upstream ULF waves and energetic electrons associated with the lunar wake: Detection of precursor activity, *Geophys. Res. Lett.*, *23*(10), 1271–1274, doi:10.1029/96GL01355.
- Farrell, W., M. Kaiser, J. Steinberg, and S. Bale (1998), A simple simulation of a plasma void: Applications to wind observations of the lunar wake, *J. Geophys. Res.*, *103*(A10), 23,653–23,660, doi:10.1029/97JA03717.
- Farrell, W. M., M. L. Kaiser, and J. T. Steinberg (1997), Electrostatic instability in the central lunar wake: A process for replenishing the plasma void?, *Geophys. Res. Lett.*, *24*(9), 1135–1138, doi:10.1029/97GL00878.
- Fatemi, S., M. Holmström, Y. Futaana, S. Barabash, and C. Lue (2013), The lunar wake current systems, *Geophys. Res. Lett.*, *40*, 17–21, doi:10.1029/2012GL054635.
- Fatemi, S., M. Holmström, Y. Futaana, C. Lue, M. R. Collier, S. Barabash, and G. Stenberg (2014), Effects of protons reflected by lunar crustal magnetic fields on the global lunar plasma environment, *J. Geophys. Res. Space Physics*, *119*, 6095–6105, doi:10.1002/2014JA019900.
- Futaana, Y., S. Machida, Y. Saito, A. Matsuoka, and H. Hayakawa (2001), Counterstreaming electrons in the near vicinity of the Moon observed by plasma instruments on board NOZOMI, *J. Geophys. Res.*, *106*, 18,729–18,740, doi:10.1029/2000JA000146.
- Futaana, Y., S. Machida, Y. Saito, A. Matsuoka, and H. Hayakawa (2003), Moon-related nonthermal ions observed by Nozomi: Species, sources, and generation mechanisms, *J. Geophys. Res.*, *108*(A1), 1025, doi:10.1029/2002JA009366.
- Halekas, J., et al. (2011), First results from ARTEMIS, a new two-spacecraft lunar mission: Counter-streaming plasma populations in the lunar wake, *Space Sci. Rev.*, *165*(1–4), 93–107, doi:10.1007/s11214-010-9738-8.
- Halekas, J. S., D. L. Mitchell, R. P. Lin, L. L. Hood, M. H. Acuña, and A. B. Binder (2002), Evidence for negative charging of the lunar surface in shadow, *Geophys. Res. Lett.*, *29*(10), 1435, doi:10.1029/2001GL014428.
- Halekas, J. S., D. A. Brain, D. L. Mitchell, and R. P. Lin (2006), Whistler waves observed near lunar crustal magnetic sources, *Geophys. Res. Lett.*, *33*, L22104, doi:10.1029/2006GL027684.
- Halekas, J. S., D. A. Brain, R. P. Lin, and D. L. Mitchell (2008), Solar wind interaction with lunar crustal magnetic anomalies, *Adv. Space Res.*, *41*(8), 1319–1324, doi:10.1016/j.asr.2007.04.003.
- Halekas, J. S., Y. Saito, G. T. Delory, and W. M. Farrell (2011), New views of the lunar plasma environment, *Planet. Space Sci.*, *14*, 1681–1694, doi:10.1016/j.pss.2010.08.011, 1st Workshop on Lunar Dust, Plasma and Atmosphere - The Next Steps (LDAP), Boulder, Colo., 27–29 Jan 2010.
- Halekas, J. S., A. R. Poppe, G. T. Delory, M. Sarantos, W. M. Farrell, V. Angelopoulos, and J. P. McFadden (2012a), Lunar pickup ions observed by ARTEMIS: Spatial and temporal distribution and constraints on species and source locations, *J. Geophys. Res.*, *117*, E06006, doi:10.1029/2012JE004107.
- Halekas, J. S., A. Poppe, G. T. Delory, W. M. Farrell, and M. Horányi (2012b), Solar wind electron interaction with the dayside lunar surface and crustal magnetic fields: Evidence for precursor effects, *Earth Planets Space*, *64*, 73–82.
- Halekas, J. S., et al. (2012c), Lunar precursor effects in the solar wind and terrestrial magnetosphere, *J. Geophys. Res.*, *117*, A05101, doi:10.1029/2011JA017289.
- Halekas, J. S., A. R. Poppe, J. P. McFadden, and K.-H. Glassmeier (2013), The effects of reflected protons on the plasma environment of the Moon for parallel interplanetary magnetic fields, *Geophys. Res. Lett.*, *40*, 4544–4548, doi:10.1002/grl.50892.
- Halekas, J. S., D. A. Brain, and M. Holmström (2015), *Moon's Plasma Wake*, pp. 149–167, John Wiley, Hoboken, N. J., doi:10.1002/9781118842324.ch9.
- Harada, Y., J. S. Halekas, A. R. Poppe, S. Kurita, and J. P. McFadden (2014), Extended lunar precursor regions: Electron-wave interaction, *J. Geophys. Res. Space Physics*, *119*, 9160–9173, doi:10.1002/2014JA020618.
- Hashimoto, K., et al. (2010), Electrostatic solitary waves associated with magnetic anomalies and wake boundary of the Moon observed by KAGUYA, *Geophys. Res. Lett.*, *37*, L19204, doi:10.1029/2010GL044529.
- Hilchenbach, M., D. Hovstadt, B. Klecker, and E. Möbius (1993), Observation of energetic lunar pick-up ions near Earth, *Adv. Space Res.*, *13*(10), 321–324, doi:10.1016/0273-1177(93)90086-Q.
- Holmström, M., M. Wieser, S. Barabash, Y. Futaana, and A. Bhardwaj (2010), Dynamics of solar wind protons reflected by the Moon, *J. Geophys. Res.*, *115*, A06206, doi:10.1029/2009JA014843.
- Kennel, C. F., and H. E. Petschek (1966), Limit on stably trapped particle fluxes, *J. Geophys. Res.*, *71*, 1–28, doi:10.1029/JZ071i001p00001.
- Lin, R. P., D. L. Mitchell, D. W. Curtis, K. A. Anderson, C. W. Carlson, J. McFadden, M. H. Acuña, L. L. Hood, and A. Binder (1998), Lunar surface magnetic fields and their interaction with the solar wind: Results from lunar prospector, *Science*, *281*, 1480–1484, doi:10.1126/science.281.5382.1480.
- Lue, C., Y. Futaana, S. Barabash, M. Wieser, M. Holmström, A. Bhardwaj, M. B. Dhanya, and P. Wurz (2011), Strong influence of lunar crustal fields on the solar wind flow, *Geophys. Res. Lett.*, *38*, L03202, doi:10.1029/2010GL046215.
- Lue, C., Y. Futaana, S. Barabash, M. Wieser, A. Bhardwaj, and P. Wurz (2014), Chandrayaan-1 observations of backscattered solar wind protons from the lunar regolith: Dependence on the solar wind speed, *J. Geophys. Res. Planets*, *119*, 968–975, doi:10.1002/2013JE004582.
- Lyon, E. F., H. S. Bridge, and J. H. Binsack (1967), Explorer 35 plasma measurements in the vicinity of the Moon, *J. Geophys. Res.*, *72*, 6113–6117, doi:10.1029/JZ072i023p06113.
- Mall, U., E. Kirsch, K. Cierpka, B. Wilken, A. Söding, F. Neubauer, G. Gloeckler, and A. Galvin (1998), Direct observation of lunar pick-up ions near the Moon, *Geophys. Res. Lett.*, *25*(20), 3799–3802, doi:10.1029/1998GL900003.
- McFadden, J. P., C. W. Carlson, D. Larson, M. Ludlam, R. Abiad, B. Elliott, P. Turin, M. Marckwordt, and V. Angelopoulos (2008), The THEMIS ESA plasma instrument and in-flight calibration, *Space Sci. Rev.*, *141*(1–4), 277–302, doi:10.1007/s11214-008-9440-2.
- Mitchell, D. L., J. S. Halekas, R. P. Lin, S. Frey, L. L. Hood, M. H. Acuña, and A. Binder (2008), Global mapping of lunar crustal magnetic fields by lunar prospector, *Icarus*, *194*, 401–409, doi:10.1016/j.icarus.2007.10.027.
- Nakagawa, T., Y. Takahashi, and M. Iizima (2003), GEOTAIL observation of upstream ULF waves associated with lunar wake, *Earth Planets Space*, *55*(9), 569–580.

- Nakagawa, T., F. Takahashi, H. Tsunakawa, H. Shibuya, H. Shimizu, and M. Matsushima (2011), Non-monochromatic whistler waves detected by Kaguya on the dayside surface of the Moon, *Earth Planets Space*, 63(1), 37–46, doi:10.5047/eps.2010.01.005, 3rd Kaguya Science Meeting on Earth, Planets and Space, Tokyo, Japan, 14–15 Jan 2009.
- Nakagawa, T., A. Nakayama, F. Takahashi, H. Tsunakawa, H. Shibuya, H. Shimizu, and M. Matsushima (2012), Large-amplitude monochromatic ULF waves detected by Kaguya at the Moon, *J. Geophys. Res.*, 117, A04101, doi:10.1029/2011JA017249.
- Ness, N. F., and K. H. Schatten (1969), Detection of interplanetary magnetic field fluctuations stimulated by the lunar wake, *J. Geophys. Res.*, 74(26), 6425–6438, doi:10.1029/JA074i026p06425.
- Ness, N. F., K. W. Behannon, C. S. Scarce, and S. C. Cantara (1967), Early results from the magnetic field experiment on lunar explorer 35, *J. Geophys. Res.*, 72, 5769–5778, doi:10.1029/JZ072i023p05769.
- Nishino, M. N., et al. (2009), Solar-wind proton access deep into the near-Moon wake, *Geophys. Res. Lett.*, 36, L16103, doi:10.1029/2009GL039444.
- Nishino, M. N., et al. (2010), Effect of the solar wind proton entry into the deepest lunar wake, *Geophys. Res. Lett.*, 37, L12106, doi:10.1029/2010GL043948.
- Nishino, M. N., et al. (2013), Type-II entry of solar wind protons into the lunar wake: Effects of magnetic connection to the night-side surface, *Planet. Space Sci.*, 87, 106–114, doi:10.1016/j.pss.2013.08.017.
- Roux, A., O. Le Contel, C. Coillot, A. Bouabdellah, B. de la Porte, D. Alison, S. Ruocco, and M. C. Vassal (2008), The search coil magnetometer for THEMIS, *Space Sci. Rev.*, 141(1–4), 265–275, doi:10.1007/s11214-008-9455-8.
- Russell, C., and M. Hoppe (1983), Upstream waves and particles, *Space Sci. Rev.*, 34(2), 155–172, doi:10.1007/BF00194624.
- Russell, C. T., and B. R. Lichtenstein (1975), On the source of lunar limb compressions, *J. Geophys. Res.*, 80, 4700–4711, doi:10.1029/JA080i034p04700.
- Saito, Y., et al. (2008), Solar wind proton reflection at the lunar surface: Low energy ion measurement by MAP-PACE Onboard SELENE (KAGUYA), *Geophys. Res. Lett.*, 35, L24205, doi:10.1029/2008GL036077.
- Saito, Y., et al. (2010), In-flight performance and initial results of Plasma Energy Angle and Composition Experiment (PACE) on SELENE (Kaguya), *Space Sci. Rev.*, 154, 265–303, doi:10.1007/s11214-010-9647-x.
- Santolik, O., D. A. Gurnett, G. H. Jones, P. Schippers, F. J. Crary, J. S. Leisner, G. B. Hospodarsky, W. S. Kurth, C. T. Russell, and M. K. Dougherty (2011), Intense plasma wave emissions associated with Saturn's moon Rhea, *Geophys. Res. Lett.*, 38, L19204, doi:10.1029/2011GL049219.
- Schubert, G., and B. R. Lichtenstein (1974), Observations of Moon-plasma interactions by orbital and surface experiment, *Rev. Geophys. Space Phys.*, 12, 592–626, doi:10.1029/RG012i004p00592.
- Tao, J. B., et al. (2012), Kinetic instabilities in the lunar wake: ARTEMIS observations, *J. Geophys. Res.*, 117, A03106, doi:10.1029/2011JA017364.
- Tsugawa, Y., N. Terada, Y. Katoh, T. Ono, H. Tsunakawa, F. Takahashi, H. Shibuya, H. Shimizu, and M. Matsushima (2011), Statistical analysis of monochromatic whistler waves near the Moon detected by Kaguya, *Ann. Geophys.*, 29(5), 889–893, doi:10.5194/angeo-29-889-2011.
- Tsugawa, Y., et al. (2012), Statistical study of broadband whistler-mode waves detected by Kaguya near the Moon, *Geophys. Res. Lett.*, 39, L16101, doi:10.1029/2012GL052818.
- Yokota, S., and Y. Saito (2005), Estimation of picked-up lunar ions for future compositional remote SIMS analyses of the lunar surface, *Earth Planets Space*, 57(4), 281–289.
- Yokota, S., et al. (2009), First direct detection of ions originating from the Moon by MAP-PACE IMA Onboard SELENE (KAGUYA), *Geophys. Res. Lett.*, 36, L11201, doi:10.1029/2009GL038185.